NMR in Biomedicine

WILEY

NMR IN BIOMEDICINE

RESEARCH ARTICLE OPEN ACCESS

Improving the Accuracy and Repeatability of Renal Stiffness Measurement With Magnetic Resonance Elastography: Influence of Vibration Frequency, Acquisition Orientation, and Postprocessing—A Phantom and Volunteer Study

Eva Jambon[1,2,3] | Camille Courtine[4] | Bruno Soulabaille[5] | David Chéchin[6] | Benjamin Robert[6] | Joffrey Sarrazin[7] | Gaëlle Margue[3,8] | Jean-Christophe Bernhard[3,8] | Yann Le Bras[1] | Amandine Crombé[1,2]

[1]Department of Radiology, Pellegrin Hospital, Bordeaux, France | [2]SARCOTARGET Team, Bordeaux Research Institute in Oncology (BRIC) INSERM U1312 and University of Bordeaux, Bordeaux, France | [3]I.CaRe Team, Bordeaux Research Institute in Oncology (BRIC) INSERM U1312 and University of Bordeaux, Bordeaux, France | [4]Centre de Recherche Paul Pascal, University of Bordeaux, Pessac, France | [5]Department of Radiology, Saint-André Hospital, Bordeaux, France | [6]Philips Healthcare France, Suresnes, France | [7]Department of Additive Fabrication Engineering, Bordeaux University Technological Institute, Gradignan, France | [8]Department of Urology, Pellegrin Hospital, Bordeaux, France

Correspondence: Amandine Crombé (amandine.crombe@chu-bordeaux.fr)

Received: 5 January 2025 | **Revised:** 16 April 2025 | **Accepted:** 23 April 2025

Funding: This work was supported by ANR-21-RHUS-0015.

Keywords: kidney imaging | magnetic resonance elastography | phantom study | sequence optimization

ABSTRACT

MR elastography (MRE) is validated for liver fibrosis but remains highly challenging for renal imaging. Our aim was to optimize a prototype MRE sequence developed by Philips Healthcare for accurate and repeatable stiffness measurement using standardized phantoms and pipeline and to translate it to in vivo kidney imaging. Hence, in this prospective single-center study, 21 silicone-based phantoms with known stiffness ranging between 2 and 57.7 kPa were imaged at 1.5-Tesla using a 2D-gradient echo MRE acquisition. Mechanical vibrations were generated through a pneumatic driver with an actuator fixed on a dedicated 3D-printed phantom container. Four frequencies (60, 80, 100, and 120 Hz), three orientations (axial, sagittal, and coronal), and three MRE postprocessing algorithms were investigated (local frequency estimation [LFE], multifrequency dual elasto-visco inversion [MDEV], and wavenumber-based MDEV [kMDEV]). Acquisitions were repeated twice and coregistered. The best combinations of frequency, orientation, and postprocessing in terms of repeatability (measured with intraclass correlation coefficient [ICC]) and accuracy (measured with using root mean square error [RMSE]) were translated on five healthy volunteer's kidneys. The lowest/best RMSE was obtained with sagittal orientation, 120 Hz and LFE (RMSE = 8.9). The highest ICC was obtained with axial orientation, 120 Hz and LFE (ICC = 0.864, $p < 0.0001$). On phantoms with stiffness < 25 kPa, the best performing combination was sagittal orientation, 60 Hz and LFE (RMSE = 4.2). Multiple-way analysis of variance showed a strong influence of frequency ($F = 47.8$, $p < 0.0001$) and postprocessing ($F = 49.5$, $p < 0.0001$), but not orientation ($p = 0.4771$). Best image quality in volunteers was obtained with coronal orientation and mechanical vibrations of 60 Hz with anterior–posterior direction and LFE.

Abbreviations: ANOVA, Analysis of variance; CKD, chronic kidney diseases; 95%CI, 95% confidence interval; E, Young's modulus of elasticity; GES, generalized eta-squared; ICC, intraclass correlation coefficient; kMDEV, wavenumber-based multifrequency dual elasto-visco inversion; LFE, local frequency estimation; MDEV, multifrequency dual elasto-visco inversion; MRE, magnetic resonance elastography; PDMS, polydimethylsiloxane; RMSE, root mean square error; ROI, region of interest; μ, shear modulus elastography; V, shear wave velocity.

In conclusion, our study showed that vibration frequency of 120 Hz provided the highest MRE accuracy across all phantoms (2–57.7 kPa), while 60 Hz was more suitable for stiffness values < 25 kPa and in vivo. Postprocessing significantly influenced stiffness values, with LFE offering superior accuracy and repeatability, whereas the orientation had minimal effect.

1 | Introduction

Magnetic resonance elastography (MRE) was first described in 1995 by Muthupillai et al. from the Mayo Clinic [1]. They developed a noninvasive technique based on motion-sensitive phase imaging, relying on the propagation of a mechanical wave through the tissue and produced by an external device, followed by the application of wave inversion algorithms to quantify the tissue stiffness. The same technique is still used today and remains the reference MRE method [2]. During the last two decades, the technique underwent significant clinical development particularly in liver diseases, facilitated by the liver proximity to the skin, allowing for the use of low-frequency vibrations [3]. For instance, regarding the quantification of liver fibrosis, a meta-analysis involving more than 3000 patients demonstrated higher diagnostic performance of MRE compared to acoustic radiation force impulse (ARFI), especially for early stages of fibrosis [4]. Thus, MRE is currently emerging as the gold standard for hepatic fibrosis quantification [5].

Regarding kidney, MRE has been far less investigated, mostly on small cohorts of animal models [6–8] and healthy adult volunteers [9–13]. These preliminary studies found highly variable renal stiffness ranging between 2.2 and 9.4 kPa in healthy kidneys [9–14]. Actually, these studies agree that many features could influence this stiffness, such as acquisition parameters (i.e., spin echo versus gradient imaging, 2D versus 3D sequence, pulse frequency, sequence orientation), the direct environment (i.e., anisotropy, digestive gas), the procedural conditions (i.e., hydration, fasting, motion artifacts) [15, 16], and postprocessing (notably the reconstruction algorithm to derive the quantitative stiffness maps from the mechanical waves propagating through the tissues) [17–19]. The few clinical studies have emphasized the potentials of MRE to distinguish subtypes of small renal tumors [20] and to estimate and monitor the renal fibrosis in chronic kidney diseases (CKD) [21–23]. However, important stiffness overlaps and standard deviations were observed between different tumors and between different CKD stages requiring more accurate MRE sequences.

Moreover, while most MRE studies focus on average stiffness values within large regions of interest (ROIs) encompassing entire kidneys or whole tumors, significant variability in stiffness can exist within these ROIs, with some voxels exhibiting values exceeding 20 kPa [20, 24]. This variability is not surprising, given the well-documented intratumoral heterogeneity observed in many cancers and the heterogeneous distribution of renal fibrosis throughout the kidney [25]. Therefore, MRE sequences and postprocessing capable of accurately capturing a range of stiffness values—high, intermediate, and low—within segmented regions could substantially enhance the diagnostic and prognostic utility of MRE by incorporating detailed textural analysis. To achieve accurate assessment across the wide range of stiffness observed in human tissues and kidney diseases, a noninvasive approach could involve investigating the correlations between MRE-derived stiffness measurements and reference stiffness values obtained using dedicated physical systems in well-calibrated phantoms.

Therefore, our aims were as follows: (i) to calibrate an optimal MRE sequence (including vibration frequency, acquisition orientation and postprocessing) capable of detecting the full spectrum of stiffness observed in both healthy and pathological kidneys with high accuracy and reproducibility using phantom of known stiffness, (ii) to understand the impact of each varying characteristics in the sequence building, and (iii) to test the best MRE sequences for kidney imaging in healthy adult volunteers.

2 | Material and Methods

This prospective observation single-center study was approved by the institutional review board of Bordeaux university hospital, France, in agreement with good clinical practice and applicable laws. Signed written informed consent was collected for each volunteer.

Figure 1 represents the overall study workflow.

2.1 | Development of Calibrated Phantoms

Twenty-one phantoms were fabricated using a same dedicated aluminum mold with a rectangular parallelepiped shape. Their dimensions were subsequently standardized at $50 \times 50 \times 60\ mm^3$. The phantoms were made at the Paul Pascal Research Center (Talence, France), using polydimethylsiloxane (PDMS), an organosilicon polymer that is widely used in biomedical engineering and microfluidics due, notably, to its flexible and elastic properties of which the stiffness can be controlled. Herein, to obtain a wide range of PDMS stiffness within each phantom, three components were mixed as follows: a platinum-catalyzed silicone rubber (reactant A, Ecoflex™ 00–20, Smooth-On Inc., Macungie, Pennsylvania, USA), a platinum-cure silicone rubber (reactant B, DragonSkin™ 10 Slow, Smooth-On Inc., Macungie, Pennsylvania, USA), and a nonreactive silicone fluid designed to control and lower the viscosity of silicone rubber products (Thinner, Smooth-On, Smooth-On Inc., Macungie, Pennsylvania, USA). The thinner component was mixed with the reactant A, before mixing the A and B reactants. The ratio of the three components mixed within each phantom is given in Table 1. Once the reactive species had been mixed together for 3 min, they were poured into the aluminum mold, degassed, and let rest for 4 h at room temperature before unmolding.

The next step was to accurately measure the reference stiffness of each phantom using the gold standard method, namely, a tensile and compression testing machine (ZwickRoell Z2.5/TN1S apparatus, ZwickRoell GmbH & Co., Ulm, Germany).

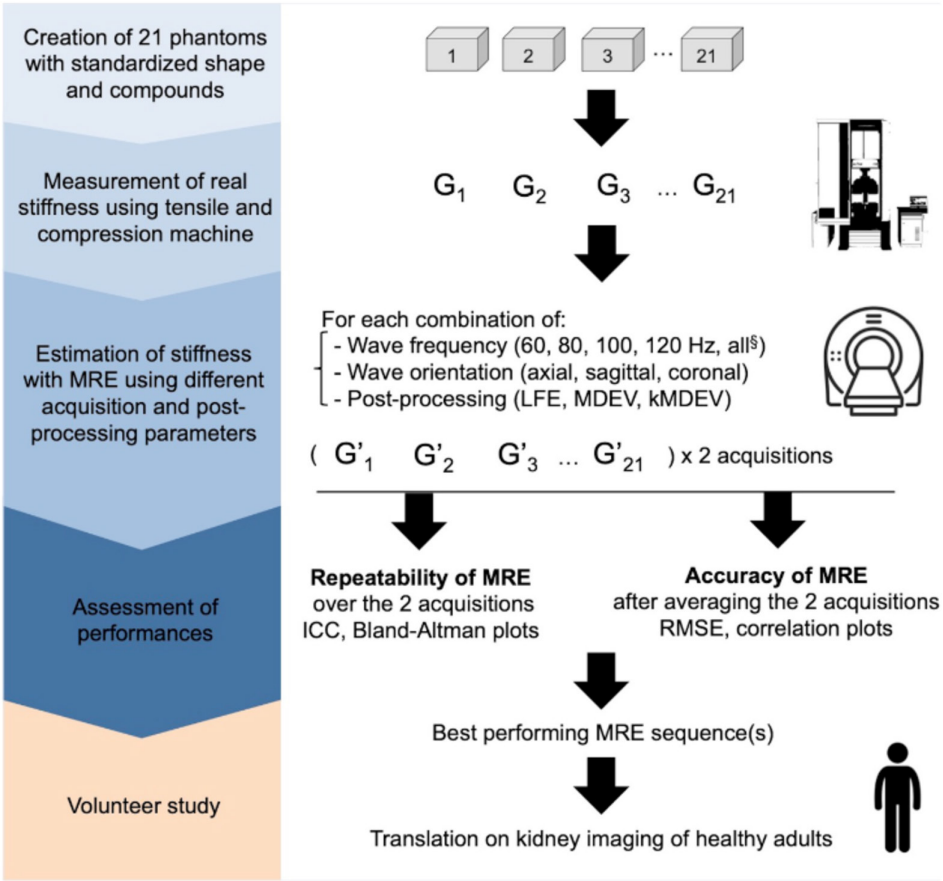

FIGURE 1 | Study workflow. Abbreviations: G, real stiffness; G', estimated stiffness; ICC, intraclass correlation coefficient; LFE, local frequency estimation; MDEV, multifrequency dual elasto-visco inversion; MRE, magnetic resonance elastography; RMSE, root mean squared error. §: the combination of all frequencies could only be postprocessed with MDEV and kMDEV.

For each formula of each phantom (Table 1), five tensile test specimens of 1.1-mm thickness, 50-mm length, and 10-mm width were prepared to conduct the tensile experiments. These specimens were produced using a dedicated mold, following the exact same formulation and during the same preparation session as the larger phantoms prepared for MRE, ensuring identical composition and mechanical properties. The tensile test specimens were specifically designed to be compatible with the ZwickRoell testing system. Subsequently, material hardness was assessed using the same machine, which applies a precisely calibrated force to the specimen's surface. The depth and shape of the resulting indentation provide quantitative information about the material's resistance to deformation, thereby offering insight into its mechanical behavior under physiological stress.

The measurements were performed at constant tensile speed of 100 mm/min. In the linear elastic regime, Hooke's law is verified as follows:

$$\sigma = E \times \varepsilon$$

where we have the following:

- $\sigma = F/S$ is the normal stress calculated from the normal force (F) and the sample cross-section area (S),
- $\varepsilon = (l - l_0)/l_0$ with l_0 and l are the sample lengths before and during tension, respectively,
- E is the Young's modulus of elasticity, which is linked to the shear modulus elastography (G) in kPa or kN/m^2, by a factor of 3 ($E = 3 \times G$), derived from the shear wave velocity (V) in m/s (i.e., $E = 3 \times \rho \times V^2$, where ρ is the tissue density) [26].

Thus, for the five tensile specimens corresponding to each phantom, the stiffness was measured and then averaged to obtain the real reference stiffness (i.e., gold standard measure) of the corresponding phantom.

2.2 | Development of a Phantom Container for Reproducible MRE Positioning and Measurement

A rigid polyvinyl chloride (PVC) container was designed to ensure consistent positioning of the phantoms and the mechanical vibration device, which includes an active pneumatic driver and a passive actuator with an 18-cm diameter (Resoundant, Inc., Mayo Clinic, Rochester, Minnesota, USA) (Figure 2). The container was designed using TinkerCad freeware (https://www.tinkercad.com/) and 3D-printed at the TechnoShop from Bordeaux university in France. It features a cylindrical shape

TABLE 1 | Preparation of the phantoms: Recipe and stiffness on corresponding tensile test specimens.

Phantom ID	Percentage of ecoflex	Percentage of thinner	Percentage of dragonskin	Measured Young modulus of elasticity (E, kPa)	Shearwave modulus - reference stiffness (G, kPa)
1	40	60	0	5.84	2.00
2	50	50	0	9.73	3.24
3	70	30	0	16.3	5.4
4	40	40	20	18.6	6.2
5	80	20	0	26	8.7
6	85	15	0	27.2	9.1
7	90	10	0	28.7	9.6
8	31	31	38	30.3	10.1
9	33	33	34	31.7	10.6
10	95	5	0	38	12.7
11	100	0	0	48.9	16.3
12	90	0	10	53.9	18.0
13	85	0	15	56.6	18.9
14	25	25	50	64.6	21.5
15	75	0	25	71.6	23.9
16	18.5	18.5	63	72.8	24.3
17	16.5	16.5	67	86.8	28.9
18	60	0	40	89.8	30.0
19	50	0	50	105	35.0
20	40	0	60	121	40.3
21	30	0	70	173	57.7

Note: The measured Young's modulus of elasticity (E, kPa) was obtained from compression testing of small standardized tensile test specimens using the ZwickRoell testing machine. The corresponding shear modulus (G, kPa), referred to as the shear wave modulus or reference stiffness, was derived using the standard linear elastic approximation $G = E/3$. These G values served as the reference stiffness values for MRE-based estimations and subsequent RMSE calculations.

tailored to accommodate the vibration device on its upper face and a parallelepiped cage at the bottom center to securely hold the phantom. The container was filled with ultrasound gel, applied in a sufficient and uniform layer around the phantom to ensure optimal coupling. Indeed, embedding the phantoms in ultrasound gel enabled to minimize magnetic susceptibility artifacts at the air–phantom interface, which could compromise MRE quality. Additionally, the ultrasound gel acted as a coupling medium that facilitates the uniform propagation of shear waves into the phantom during mechanical excitation. It also provided mechanical stability, preventing unwanted displacement of the phantom during image acquisition. Finally, this setup helped to simulate a soft tissue-like environment, ensuring more physiologically relevant experimental conditions.

2.3 | MRE Acquisitions in Phantoms

The MRI experiments were conducted on a same 1.5-Tesla MR-system (Achieva dSTREAM, Philips Medical Systems, Best, the Netherlands). The phantom was placed inside the container, surrounded and covered with ultrasound gel, and the vibration device was then placed on top. The entire setup was then secured within the head coil (with 16 elements) and immobilized using gel pads and weighted wedges.

A rapid T2-weighted sequence (single shot turbo spin echo) was utilized to localize the phantom.

The MRE sequence was a prototypal work-in-progress sequence provided by Philips Healthcare with the possibility to utilize various frequencies of the mechanical vibration, motion-sensitizing gradient direction, and motion-sensitizing gradient strength. Herein, it corresponded to a multislice 2D gradient echo sequence (fast field-echo) with a repetition time of 50 ms, an echo time of 12 ms, a field-of-view of $250 \times 219 \times 29\,mm^3$, three slices with a slice thickness of 10 mm, and an acquired voxel size of $1.5 \times 4.68 \times 10\,mm^3$. Mechanical vibrations with low amplitude and different frequencies (60, 80, 100, and 120 Hz) were generated thanks to

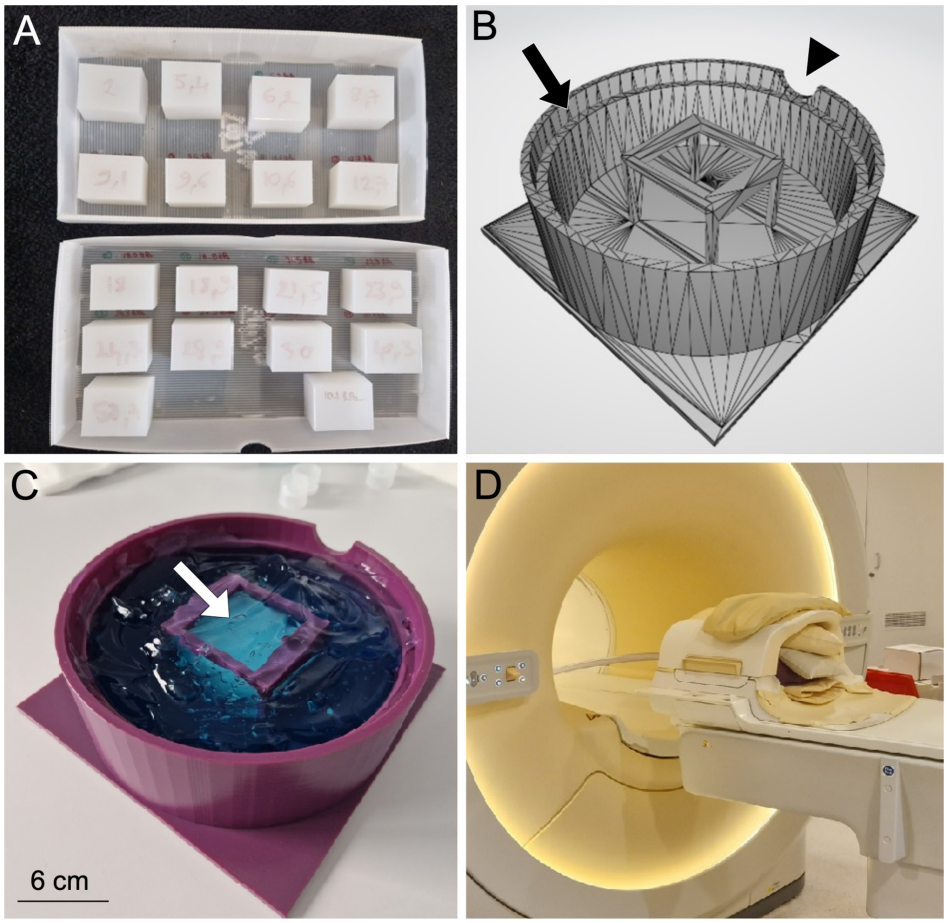

FIGURE 2 | Development of a standardized phantom container to ensure reproducible magnetic resonance elastography (MRE) acquisition and stiffness measurements. (A) Phantoms with standardized composition, shape and size ($5 \times 5 \times 6\,cm^3$). (B) Technical drawing of the phantom container. The upper side was open with a cylindrical shape of a same diameter (18 cm) as the device generating the mechanical vibration with a stop to prevent its movement (black arrow) and a small rounded notch for the cable to pass through (black arrowhead). (C) 3D-printing of the phantom container. The phantom was inserted in the central cage (white arrow) and the container was filled with ultrasound gel, applied in a sufficient and uniform layer around the phantom to ensure optimal coupling. (D) MRE acquisition inside the head coil with pads to all around the container and coil to prevent motion.

the device described above fixed on the phantom container. This MRE sequence was then acquired in the axial, sagittal, and coronal planes for each phantom, at each different frequency. Each phantom underwent two full MRI examinations during two separate sessions in order to assess the repeatability of the sequence.

2.4 | MRE Reconstruction and Analysis

Three inversion methods were investigated to perform the MRE postprocessing: *(i)* local frequency estimation (LFE) [17], *(ii)* multifrequency dual elasto-visco inversion (MDEV) [18], and *(iii)* wavenumber-based MDEV (kMDEV) [19]. Briefly, LFE is the standard, fastest, and simplest algorithm that estimates stiffness based on local frequency of shear waves. Its limitation is a possible low accuracy in regions with complex wave patterns and noise [17]. MDEV is a more advanced algorithm that directly solves the Helmholtz equation (a partial differential equation describing how mechanical waves propagate in a medium) and is supposed to provide higher resolution and more accurate stiffness map [18]. KMDEV is k-space extension of MDEV with an improved precision and noise resistance incorporating multiscale information [19].

The LFE-based maps were reconstructed on the acquisition console using the dedicated commercially available algorithms supplied by Philips Healthcare (MREView software, v5.7) and producing amplitude, phase, colorized wave propagation, and elastogram images. A confidence mask automatically excluded voxels with a $< 95\%$ threshold confidence index.

The MDEV and kMDEV postprocessing were achieved using the free online application provided by the Charité - Universitätsmedizin Berlin on their public server (https://bioqic-apps.charite.de/). These inversion methods produced a magnitude of complex shear modulus map (absG-map, in kPa) for MDEV and a shear wave velocity map (c-map, in m/s) for kMDEV. As the shear wave velocity (V) is directly proportional to the stiffness (μ), as expressed by the formula $\mu = \rho \times V^2$ (with a known phantom density $\rho = 1.070\,kg/m^3$), the stiffness map could be easily reconstructed by applying it to each voxel from the shear wave velocity map. The MDEV and kMDEV postprocessing were applied on individual frequency and also on their

combination (i.e., the MRE acquisitions performed for 60, 80, 100, and 120 Hz were processed altogether in the algorithms providing "all-frequency" stiffness maps).

Afterwards, the stiffness maps were exported in the nifti format and coregistered altogether (for a given frequency and a given orientation) using a rigid coregistration ("extranstr" package, https://github.com/muschellij2/extrantsr) in R (v4.1.0, the R foundation for statistical computing, Vienna, Austria).

Next, the postprocessed images were imported to the LIFEx freeware (v7.4.0, Saclay, France) [27]. A senior board-certified radiologist with 10 years of experience in MRI (E.J.) manually placed a squared 2D region-of-interest (ROI) of $10 \times 10\,mm^2$ in the center of the phantom on the stiffness map from the first session LFE and propagated it onto the other stiffness maps from the two sessions created with the other algorithms. The correct ROI propagation was systematically verified manually by the radiologist. The mean stiffness value inside the ROI was then exported.

2.5 | MRE in Healthy Volunteers

Then, the optimal MRE sequences (i.e., optimal combinations of vibration frequency, orientation and postprocessing to reach the highest accuracy and repeatability) were transposed for kidney imaging in five healthy adult volunteers. The left and the right kidneys were imaged separately. The patients were positioned on dorsal decubitus with the vibration device placed on the lumbar fossa of the homolateral kidney.

The abdominal coil (with eight elements) was placed on the abdominal wall and the spine coil (with 8 elements, integrated in the MRI table, was also activated). Acquisition parameters were field-of-view = 200×180 mm2, matrix = 240×240, initial voxel size = $2.5 \times 3\,mm^2$ (reconstructed voxel size = $0.83 \times 0.83\,mm^2$) TE = 25 msec, TR = 50 msec, flip angle = 25°, high amplitude of the mechanical vibration, no parallel imaging, and one repetition. The other acquisition and postprocessing parameters were determined according to the results of the phantom experiments.

Presaturation bands were positioned below the kidney and at its medial and lateral faces, and motion encoding gradients were applied in the slice-select direction.

One stack of three slices of 15-mm thickness per slice was acquired twice during 18-s breath-holds.

Two radiologists (A.C. and E.J., with 14 and 10 years of experience in MRI, respectively) reviewed the image quality and manually segmented the whole kidneys in consensus on the stiffness maps to extract the average renal stiffness.

2.6 | Statistical Analysis

Statistical analyses were also performed in R. All tests were two-tailed. A *P*-value less than 0.05 was deemed significant.

2.6.1 | Repeatability of the Stiffness Measurements in Phantoms

The repeatability of MRE stiffness measurements across the 21 phantoms was assessed for each combination of vibration frequency, orientation, and postprocessing method using the intraclass correlation coefficient (ICC) with a 95% confidence interval (95% CI). The analysis employed a "one-way" model with "consistency" type and "single" unit settings ("irr" package, https://github.com/cran/irr). ICC values were interpreted as follows: 0 to 0.50 indicates poor reproducibility, 0.50 to 0.75 moderate reproducibility, 0.75 to 0.90 good reproducibility, 0.90 to 0.99 excellent reproducibility, and an ICC of 1 reflects perfect reproducibility. The Bland–Altman plot for the best combination was drawn [28].

2.6.2 | Accuracy of the Stiffness Measurements in Phantoms

The mean stiffness obtained during the two acquisitions performed for each phantom and for each combination of frequency, orientation and postprocessing was averaged for this analysis.

Afterwards, for each combination of frequency, orientation, and postprocessing, the root mean square error (RMSE) was calculated to estimate the accuracy of the MRE acquisitions over the 21 phantoms compared to the reference stiffness obtained with the tensile and compression testing machine, as follows:

$$\mathrm{RMSE}_{(\mathrm{frequence,orientation,postprocessing})} = \sqrt{\sum_{i=1}^{n} \frac{\left(\mathrm{Stiffness}_{\mathrm{MRE}} - \mathrm{Stiffness}_{\mathrm{Reference}}\right)^2}{n}}$$

The 95%CI for the RMSE was determined by bootstrapping the results with 1000 replicates of the initial population ("boot" package, https://github.com/cran/boot/).

The analyses of accuracy and repeatability were also performed in the subgroup of phantoms ranging from 0 to 25 kPa (i.e., the stiffness range most frequently encountered in oncology).

2.6.3 | Features Influencing the Stiffness Measurements in Phantoms

Next, the factors influencing the stiffness measurements were examined using a three-way repeated-measures ANOVA. The potential explanatory factors included postprocessing (LFE, MDEV, and kMDEV), frequency (60, 80, 100, or 120 Hz), and slice orientation (axial, coronal, or sagittal) ("rstatix" R package, https://github.com/kassambara/rstatix). Effect sizes were quantified using generalized eta-squared (GES), which represents the proportion of total variance explained by each factor, accounting for the overall design of the experiment. GES was calculated to provide a generalizable measure of effect size across different conditions.

Figures were created using the 'ggplot2' and 'cowplot' packages (https://github.com/tidyverse/ggplot2 and https://github.com/wilkelab/cowplot).

3 | Results

A total of 1764 stiffness maps were calculated for 21 phantoms with real stiffness ranging between 2 and 57.7 kPa, including 18 phantoms with real stiffness < 25 kPa. (Figure 1). There was a total of 42 combinations of parameters. No acquisition had to be removed during the quality control. Figure 3 shows a typical image dataset for one phantom.

3.1 | Repeatability of Stiffness Measurements on Phantom Acquisitions

Figure 4A shows the ICC obtained each pair of acquisitions, and Table 2 provides the 10 highest ICCs. The highest ICCs and the MRE parameters were the following: (1) ICC = 0.864 (95%CI: 0.699–0.942, $p < 0.0001$) for frequency = 120 Hz, axial orientation, and LFE postprocessing; (2) ICC = 0.691 (95%CI: 0.386–0.861, $p = 0.0001$) for frequency = 60 Hz, axial orientation, and LFE postprocessing; and (3) ICC = 0.676 (95%CI: 0.362–0.854, $p = 0.0002$) for frequency = 100 Hz, axial orientation, and LFE postprocessing. Conversely, the lowest ICC was reached with the combination of all frequencies, coronal orientation, and MDEV postprocessing (ICC = −0.305 (95%CI: −0.640–0.132, $p = 0.9178$).

Figure 4B shows the Bland–Altman plot for the combination with highest ICC demonstrating no proportional or systematic bias.

3.2 | Precision of Stiffness Measurements on Phantom Acquisitions

Figure 4C shows that the ICC obtained each pair of acquisitions, and Table 2 also provides the 10 lowest RMSEs. The acquisitions that minimized the errors between real and estimated stiffness were as follows: (1) RMSE = 8.9 (95%CI: 6.8–12.8) for frequency = 120 Hz, sagittal orientation and LFE postprocessing; (2) RMSE = 9.0 (95%CI: 6.9–12.9) for frequency = 60 Hz, axial orientation and kMDEV postprocessing; and (3) RMSE = 9.6 (95%CI: 7.3–13.8) for frequency = 60 Hz, sagittal orientation and kMDEV postprocessing.

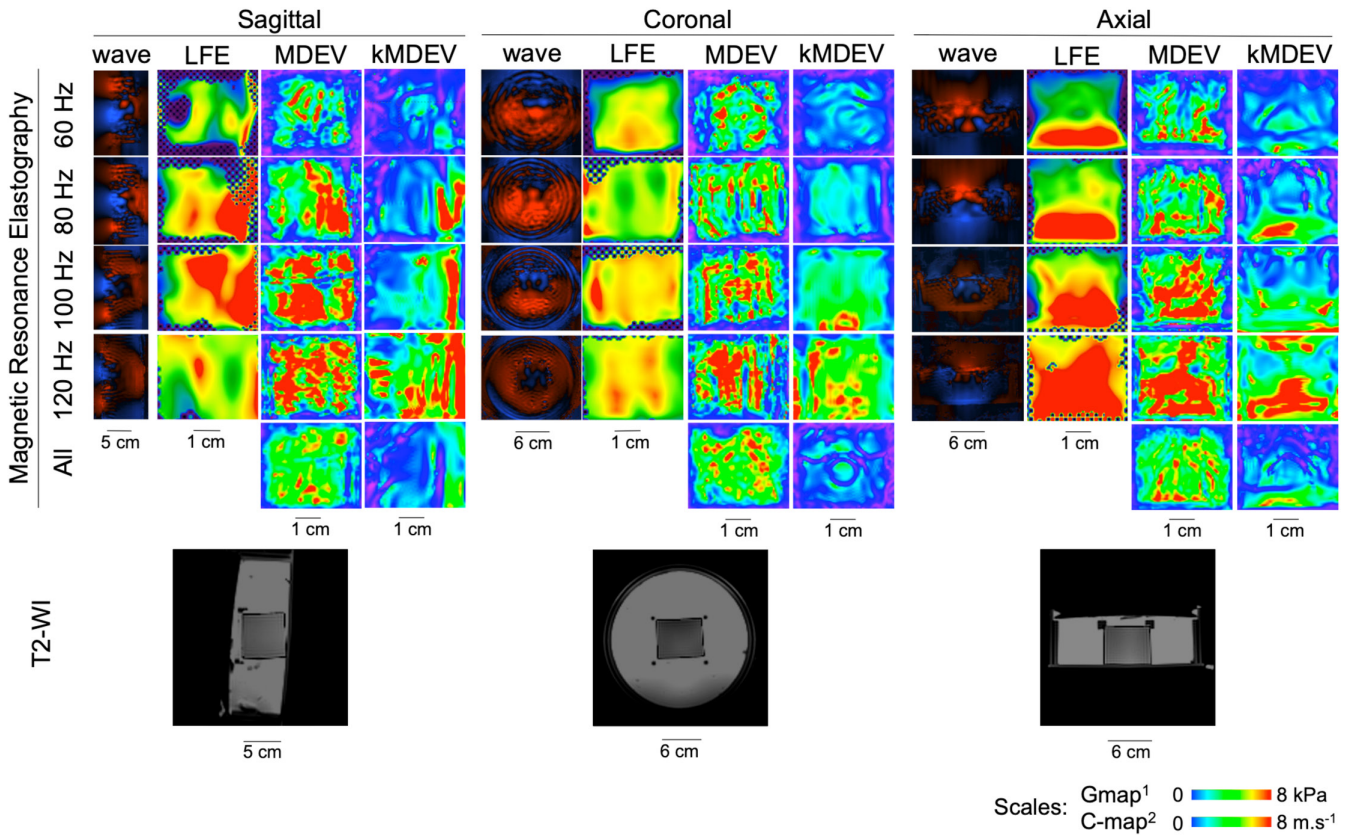

FIGURE 3 | Example of an image dataset obtained for one phantom and one of the two acquisition sessions. Herein, the phantom had a real stiffness of 4 kPa. Four frequencies of the mechanical vibrations were investigated (i.e., 60, 80, 100, and 120 Hz)—displayed on the rows, as well as three orientations (axial, coronal and sagittal) and three postprocessing algorithms (LFE, MDEV and kMDEV) as well as the wave image—displayed on columns. In addition, all frequencies could be included in the MDEV and kMDEV algorithms, which provided the 'All' (frequencies) map. The last row correspond to the T2-weighted imaging (WI) of the phantom. [1]: scale for LFE and MDEV, [2]: scale for kMDEV. The size scale is given at the bottom of the columns.

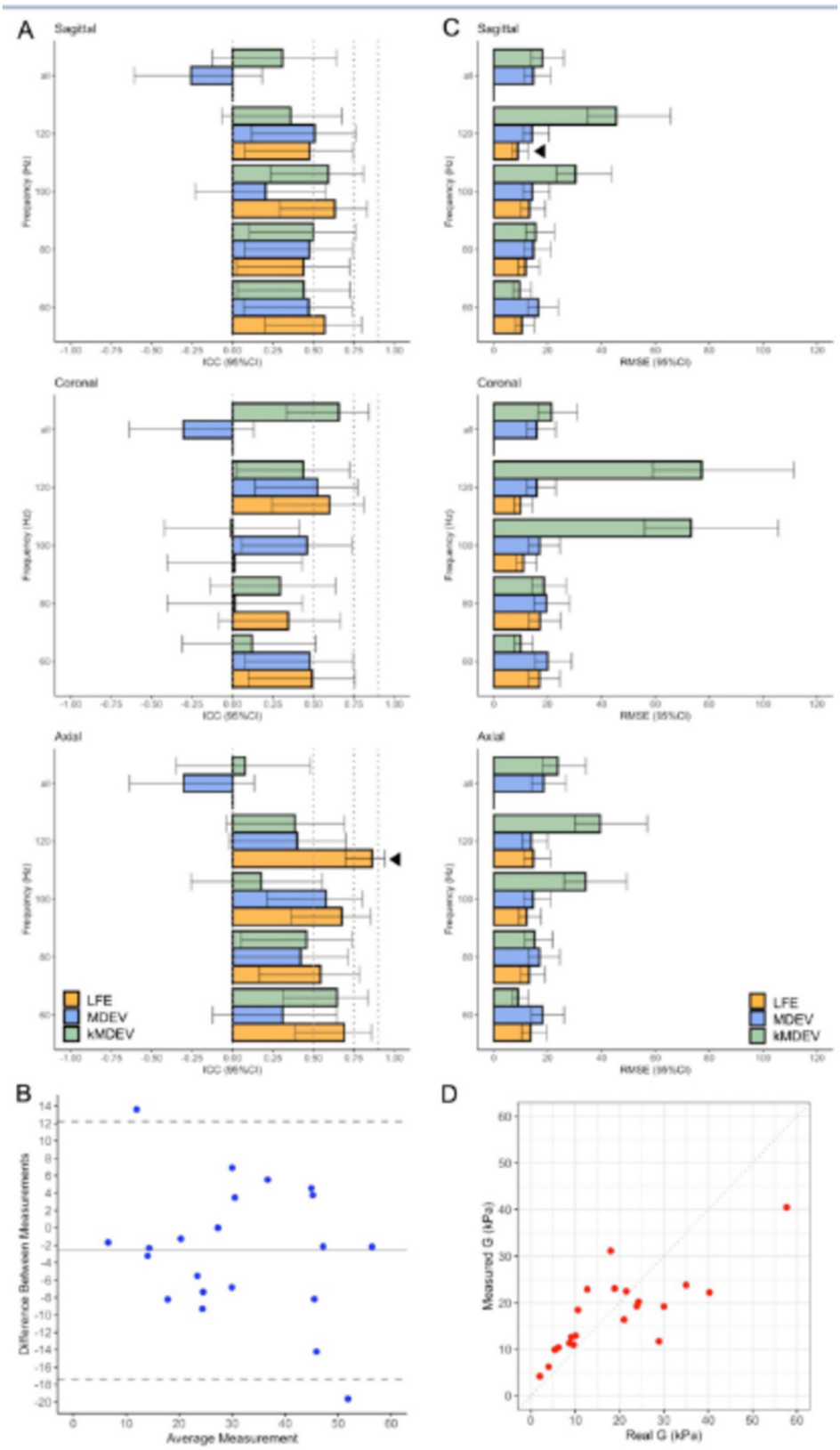

FIGURE 4 | Performances of the MRE sequences on the 21 phantoms. (A) Intraclass correlation coefficients (ICC) with 95% confidence intervals (95%CI) depending on the wave orientation, wave frequency and postprocessing. The dotted lines represent the usual cut-offs (0.5, 0.75 and 0.9) to qualify ICC. A black arrowhead indicates the combination providing the highest ICC. (B) Bland Altman plot for this best combination (frequency = 120 Hz, axial orientation, LFE postprocessing) showing that 19 out of 21 points remain in the limits of agreements without systematic or proportional bias. (C) Root mean squared error (RMSE, with 95%CI) depending on the wave orientation, wave frequency and postprocessing. A black arrowhead also indicates the combination providing the lowest RMSE. (D) Correlation plot between the real and measured stiffness (G and G') of this best combination (frequency = 120 Hz, sagittal orientation, LFE postprocessing).

TABLE 2 | Ten best performing combinations of acquisition and postprocessing parameters in terms of repeatability and accuracy for stiffness measurements on the 21 phantoms.

Repeatability	Rank	Frequency	Postprocessing	Orientation	ICC (95%CI)	*p*-value
	1	120	LFE	Axial	0.864 (0.699–0.942)	< 0.0001***
	2	60	LFE	Axial	0.691 (0.386–0.861)	0.0001***
	3	100	LFE	Axial	0.676 (0.362–0.854)	0.0002***
	4	All	kMDEV	Coronal	0.657 (0.332–0.844)	0.0004***
	5	60	kMDEV	Axial	0.646 (0.315–0.839)	0.0005***
	6	100	LFE	Sagittal	0.633 (0.294–0.832)	0.0006***
	7	120	LFE	Coronal	0.600 (0.245–0.815)	0.0013**
	8	100	kMDEV	Sagittal	0.593 (0.234–0.811)	0.0015**
	9	100	MDEV	Axial	0.578 (0.214–0.803)	0.0020**
	10	60	LFE	Sagittal	0.570 (0.203–0.799)	0.0024**
Accuracy	Rank	Frequency	Postprocessing	Orientation	RMSE (95%CI)	
	1	120	LFE	Sagittal	8.9 (6.8–12.8)	—
	2	60	kMDEV	Axial	9 (6.9–12.9)	—
	3	60	kMDEV	Sagittal	9.6 (7.3–13.8)	—
	4	120	LFE	Coronal	10 (7.6–14.4)	—
	5	60	kMDEV	Coronal	10 (7.7–14.5)	—
	6	60	LFE	Sagittal	10.4 (7.9–15)	—
	7	100	LFE	Coronal	11 (8.4–15.9)	—
	8	80	LFE	Sagittal	11.8 (9–17)	—
	9	100	LFE	Axial	12.2 (9.3–17.6)	—
	10	80	LFE	Axial	13.2 (10.1–19)	—

Abbreviations: 95%CI, 95% confidence interval; ICC: intraclass correlation coefficient; LFE, local frequency estimation; MDEV, multifrequency dual elasto-visco inversion; RMSE, root mean square error.
*$p < 0.05$.
**$p < 0.005$.
***$p < 0.001$.

Conversely, the highest RMSE was 77.2 (95%CI: 59–111.4) and found for frequency = 120 Hz, coronal orientation, and kMDEV postprocessing. Figure 4D shows the correlation plot for the best combination.

3.3 | Repeatability and Precision Subanalyses on Phantoms With Real Stiffness < 25 kPa

Table 3 and Figure 5 display the results of the subanalyses on phantoms with real stiffness < 25 kPa. The setting that provided the highest repeatability (ICC = 0.868, 95%CI: 0.671–0.951, $p < 0.0001$) was frequency = 100 Hz, axial orientation, and LFE postprocessing. The best setting on the full range of stiffness obtained the third rank in this subanalysis, that is, ICC = 0.804 (95%CI: 0.534–0.926, $p < 0.0001$) for frequency = 120 Hz, axial orientation, and LFE postprocessing.

Regarding measurement accuracy, the best performing combination was frequency = 60 Hz, sagittal orientation, and LFE postprocessing and provided RMSE = 4.2 (95%CI: 3.1–6.5). The best setting on the full range of stiffness obtained the ninth rank in this subanalysis, that is, RMSE = 5.6 (95%CI: 4.1–8.6) for frequency = 120 Hz, sagittal orientation, and LFE postprocessing.

3.4 | Factors Influencing the Stiffness Measurement on Phantom Acquisitions

Table 4 shows the three-way ANOVA outputs. The most influential characteristics on stiffness were in descending order as follows: the postprocessing ($F = 49.5$, GES = 0.377, $p < 0.0001$), followed by the frequency of the mechanical vibration ($F = 47.8$, GES = 0.218, $p < 0.0001$), the interaction between the frequency and postprocessing ($F = 23.2$, GES = 0.173, $p < 0.0001$), the interaction between the frequency and the postprocessing ($F = 9.5$, GES = 0.049, $p = 0.0049$), and the interaction between the frequency and the orientation (F = 5.01, GES = 0.018, $p = 0.0162$). The orientation alone and the interaction between the three explanatory variables (i.e., frequency, orientation, and postprocessing) were not significant ($p = 0.4771$ and $p = 0.0580$, respectively).

TABLE 3 | Ten best performing combinations of acquisition and postprocessing parameters in terms of repeatability and accuracy for stiffness measurements on the 18 phantoms with real stiffness < 25 kPa.

Repeatability	Rank	Frequency	Postprocessing	Orientation	ICC (95%CI)	*p*-value
	1	100	LFE	Axial	0.868 (0.671–0.951)	0
	2	100	LFE	Sagittal	0.849 (0.629–0.944)	0
	3	120	LFE	Axial	0.804 (0.534–0.926)	0
	4	All	kMDEV	Coronal	0.797 (0.52–0.923)	0
	5	120	kMDEV	Coronal	0.724 (0.383–0.893)	0.0004
	6	80	LFE	Axial	0.709 (0.356–0.887)	0.0005
	7	100	MDEV	Axial	0.673 (0.295–0.871)	0.0012
	8	120	MDEV	Sagittal	0.669 (0.287–0.869)	0.0013
	9	80	MDEV	Sagittal	0.648 (0.254–0.86)	0.0019
	10	60	LFE	Axial	0.644 (0.248–0.858)	0.0021
Accuracy	Rank	Frequency	Postprocessing	Orientation	RMSE (95%CI)	
	1	60	LFE	Sagittal	4.2 (3.1–6.5)	—
	2	60	kMDEV	Sagittal	4.7 (3.5–7.3)	—
	3	60	LFE	Axial	4.9 (3.6–7.6)	—
	4	80	MDEV	Sagittal	5 (3.7–7.7)	—
	5	60	kMDEV	Coronal	5.2 (3.9–8.1)	—
	6	120	MDEV	Sagittal	5.3 (3.9–8.2)	—
	7	100	MDEV	Axial	5.5 (4.1–8.5)	—
	8	120	LFE	Sagittal	5.6 (4.1–8.6)	—
	9	All	MDEV	Sagittal	5.6 (4.1–8.6)	—
	10	100	LFE	Coronal	5.6 (4.1–8.6)	—

Abbreviations: 95%CI, 95% confidence interval; ICC: intraclass correlation coefficient; LFE, local frequency estimation; MDEV, multifrequency dual elasto-visco inversion; RMSE, root mean square error.
*$p < 0.05$.
**$p < 0.005$.
***$p < 0.001$.

3.5 | Translation on Volunteers

The LFE postprocessing consistently ranked the highest and was therefore selected for use with the five volunteers. While the axial and sagittal orientations showed promising performance, the three-way ANOVA indicated only a moderate influence of orientation. Additionally, the limited kidney coverage in axial and sagittal views, combined with the increased susceptibility to motion and artifacts from the nearby digestive tract, led us to select the coronal view with an anterior–posterior wave direction. Two frequencies were identified as relevant: 120 Hz for the full range of stiffness values and 60 Hz for the 0–25 kPa range. These two combinations were tested in five healthy volunteers (three men, median age: 25 years, range: 23–26). From a qualitative perspective, both radiologists consistently preferred the MRE at 60 Hz over 120 Hz, as it provided a more anatomically realistic view, with less distortion, fewer uncalculated voxels, and better differentiation between the renal medulla and cortex (Figure 6).

The mean stiffness of the right kidney was 1.88 ± 0.97 kPa at 60 Hz and 1.81 ± 0.72 kPa at 120 Hz, while for the left kidney, the mean stiffness was 2.26 ± 1.04 kPa at 60 Hz and 2.79 ± 1.39 kPa at 120 Hz.

4 | Discussion

This study presents a comprehensive evaluation of MRE sequence parameters for acquisition and postprocessing using a systematic phantom-based approach followed by translation to kidney imaging of healthy volunteers. Our results demonstrate that frequencies of the mechanical vibration and postprocessing method have the most significant influence on the stiffness values and that the best setting in in vivo human kidney corresponded to the coronal view, antero-posterior vibration with a 60-Hz frequency postprocessed with the LFE algorithm.

First, the phantom experiments highlighted key factors influencing the accuracy and repeatability of MRE measurements. The choice of postprocessing method had the most significant impact on stiffness measurements, as evidenced by the highest GES in the ANOVA results. The LFE algorithm consistently

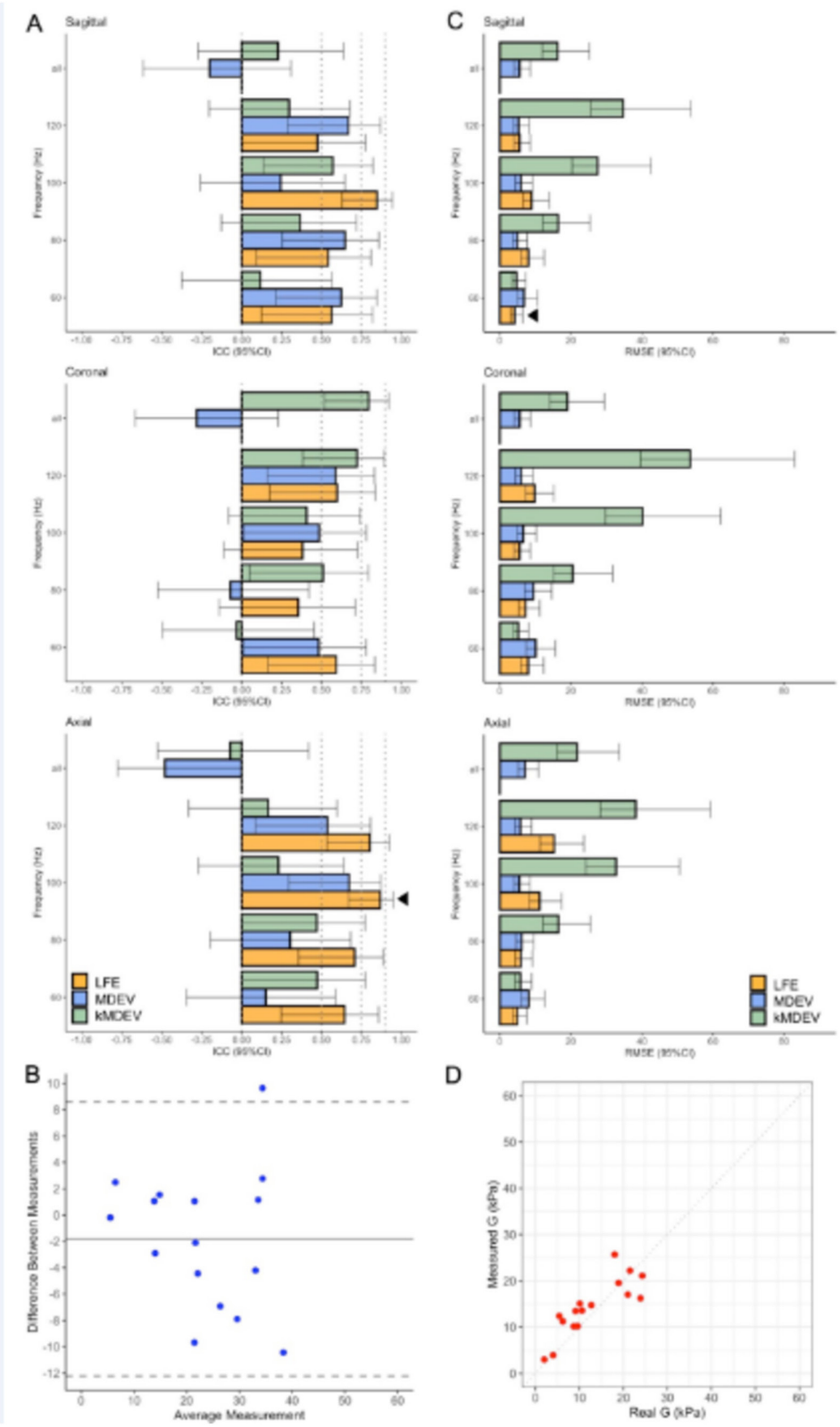

FIGURE 5 | Performances of the MRE sequences on the 18 phantoms with lower stiffness (< 25 kPa). (A) Intraclass correlation coefficients (ICC) with 95% confidence intervals (95%CI) depending on the wave orientation, wave frequency and postprocessing. The dotted lines represent the usual cut-offs (0.5, 0.75 and 0.9) to qualify ICC. A black arrowhead indicates the combination providing the highest ICC. (B) Bland Altman plot for this best combination (frequency = 100 Hz, axial orientation, LFE postprocessing) showing that 17 out of 18 points remain in the limits of agreements without systematic or proportional bias. (C) Root mean squared error (RMSE, with 95%CI) depending on the wave orientation, wave frequency and postprocessing. A black arrowhead also indicates the combination providing the lowest RMSE. (D) Correlation plot between the real and measured stiffness (G and G′) of this best combination (frequency = 60 Hz, sagittal orientation, LFE postprocessing).

outperformed other methods, particularly in terms of repeatability. The frequency of applied vibrations was the second most influential factor. Interestingly, different frequencies performed optimally depending on the stiffness range, with 120 Hz of performing best across the full range (0–57.7 kPa) and 60 Hz performing best for the 0–25 kPa range, which may be more clinically relevant for both renal tumors and renal failure and fibrosis. The MDEV method appeared less reliable across all stiffness measurements, while kMDEV showed limitations for lower stiffness values but performed better at higher stiffnesses.

TABLE 4 | Summary of the three-way repeated-measures analysis of variance ANOVA to investigate the impact of the frequency, orientation, and postprocessing on the measured stiffness of the 21 phantoms.

Effect	*F*-value	*p*-value	GES
Frequency	47.8	< 0.0001***	0.218
Orientation	0.6	0.4771	0.001
Postprocessing	49.5	< 0.0001****	0.377
Frequency: orientation	5.0	0.0162*	0.018
Frequency: Postprocessing	23.2	< 0.0001***	0.173
Orientation: Postprocessing	9.5	0.0049**	0.049
Frequency: Orientation: Postprocessing	3.2	0.0580	0.023

Note: The colons between two characteristics indicate that the studied effect corresponds to their interaction.
Abbreviation: GES, generalized eta-squared
*$p < 0.05$.
**$p < 0.005$.
***$p < 0.001$.

These findings are consistent with the study by Meyer et al. [29], which demonstrated the ability of kMDEV to differentiate high stiffness inclusions due to its kernel density estimation-based calculation and higher spatial resolution [30].

The increase in measured stiffness with increasing frequency, independent of orientation and postprocessing, is consistent with previous studies on healthy volunteers and kidney transplant recipients [10, 13, 15], likely due to the dispersive and viscoelastic properties of renal tissue.

While less impactful than postprocessing and frequency, the orientation of image acquisition slightly influenced results, particularly in interaction with other parameters. These findings underscore the importance of carefully selecting and optimizing MRE parameters for specific applications and tissue types.

Regarding MRE repeatability, the high ICCs achieved, particularly for the 120 Hz—axial orientation—LFE combination (ICC = 0.864), demonstrate the potential for excellent repeatability in renal MRE, which is crucial for longitudinal studies and monitoring disease progression or treatment response.

Interestingly, the standardized phantom set and 3D-printed container could be reused to calibrate MRE sequences in future studies and to ensure consistency of MRE measurements across different MR systems or over time, both in clinical practice and in multicenter or longitudinal studies.

Regarding the clinical translation from phantoms to human kidney imaging, our tests on healthy volunteers helped refine the sequence for the inhomogeneous conditions of the kidney within the retroperitoneum. Indeed, we observed that the 60-Hz frequency provided superior image quality and anatomical detail compared to 120 Hz, despite the latter's better performance

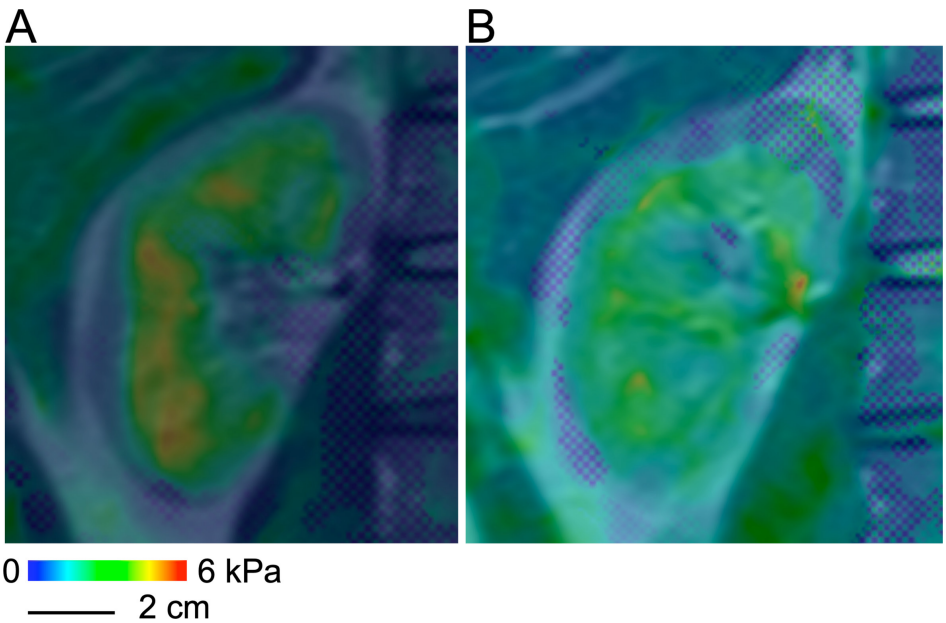

FIGURE 6 | Application of the best MRE combinations for kidney imaging in a healthy volunteer. Coronal views of the right kidney are shown with: (A) a frequency of 60 Hz, anterior–posterior orientation, and LFE postprocessing; and (B) a frequency of 120 Hz, anterior–posterior orientation, and LFE postprocessing. T2-weighted imaging was overlaid in the background with 30% opacity to visualize kidney deformation and stiffness decay captured by MRE.

in phantoms. This highlights the importance of in vivo factors such as tissue complexity and physiological motion when translating phantom results to clinical applications. The coronal orientation was preferred for kidney imaging due to better anatomical coverage and reduced susceptibility and motion artifacts, despite not being the top-performing orientation in phantom studies. This underscores the need to balance technical performance with practical clinical considerations. The measured kidney stiffness values in healthy volunteers (ranging from 1.81 to 2.79 kPa, i.e., < 5 kPa) are consistent with previous literature reports [11, 12, 31], providing initial validation of our optimized protocol. However, the low stiffness of healthy kidneys limits our ability to assess the sequence performance at higher stiffness values, which may be encountered in pathological conditions. This highlights the need for further studies including patients with various renal pathologies.

The virtual elastography technique using diffusion-weighted imaging (DWI), developed by Le Bihan et al. on 3 T-MR systems, could present an interesting alternative to traditional MRE [32]. Adapting DWI elastography for kidney imaging could help overcome some of the limitations of standard MRE, particularly in terms of availability and reproducibility. It also allows for respiratory gating and may benefit from enhanced image resolution, thanks to artificial intelligence algorithms already in use for conventional DWI and reduced field-of-view DWI [33]. However, the equation used to estimate stiffness from signal intensities across different *b*-values may need to be adjusted for kidney imaging, different magnetic field strengths, and specific *b*-values. Further studies will be required to optimize these parameters, with MRE serving as the reference standard for in vivo imaging.

Our study has limitations. First, the phantom materials, while carefully selected to mimic a range of tissue stiffnesses, cannot fully replicate the complex mechanical properties of kidney tissue. Future work could explore more sophisticated tissue-mimicking materials or ex vivo kidney samples. Second, other frequencies, combinations of frequencies, and nature of MRE sequence (notably, spin echo-echo planar imaging MRE) could have been tested in the phantom study [11]. Third, the small number of healthy volunteers limits the generalizability of our in vivo findings. Larger studies including patients with various renal pathologies are needed to fully validate the clinical utility of our optimized protocol. Fourth, alternative inversion algorithms could have been explored. For example, artificial neural networks have been trained and compared to conventional direct inversion techniques, demonstrating comparable or superior performance, with more stable stiffness maps and reduced test–retest variability [34]. More recently, Ma et al. advanced deep learning-based MRE analysis by integrating optimization-based displacement extraction with a novel traveling wave expansion-based neural network. This network was trained on simulated wave data across varying noise levels and combined with multifrequency and multidirectional data fusion to enhance shear modulus mapping. Their method showed minimal error compared to conventional techniques in both liver and brain applications [35]. In parallel, McGarry et al. developed a transverse isotropic nonlinear inversion (TI-NLI) approach to better account for tissue anisotropy, particularly in the brain. This method uses a specialized finite element model to simulate direction-dependent wave propagation along and across fiber tracts, resulting in reduced artifacts and improved stiffness estimation accuracy [36]. However, it should be noted that we selected LFE, MDEV, and kMDEV for this study due to their availability via a publicly accessible and user-friendly web-based platform, unlike the aforementioned advanced methods, which are not currently available for public use.

In conclusion, our systematic approach to optimizing renal MRE-combining phantom studies with in vivo adaptation lays a foundation for future clinical applications and deepens understanding of how acquisition and postprocessing choices impact MRE results. The identified optimal parameters enhance both the accuracy and repeatability of kidney stiffness measurements. As renal MRE technology advances, this work may support its development into a robust, noninvasive tool for assessing kidney structure and function in various pathologies.

Acknowledgments

As part of the Digital Urology 3D project (www.digital-urology-3d.fr,) this work has benefited from a government grant managed by the French national research agency (ANR) under the third investment program for the future (PIA), part of France 2030, reference ANR-21-RHUS-0015.

This study was also achieved in the framework of the University of Bordeaux's France 2030 program/RRI "IMPACT".

The authors would like to thank the radiographers from the department of Radiology of Saint-André Hospital in Bordeaux, France, for their availability and generous support.

Conflicts of Interest

B.M. and D.C. were employees at Philips Healthcare during the study period. The authors declare no conflicts of interest.

Data Availability Statement

The data that support the findings of this study are available from the corresponding author upon reasonable request.

References

1. R. Muthupillai, D. J. Lomas, P. J. Rossman, J. F. Greenleaf, A. Manduca, and R. L. Ehman, "Magnetic Resonance Elastography by Direct Visualization of Propagating Acoustic Strain Waves," *Science* 269, no. 5232 (1995): 1854–1857.

2. L. Gao, K. J. Parker, R. M. Lerner, and S. F. Levinson, "Imaging of the Elastic Properties of Tissue—A Review," *Ultrasound in Medicine and Biology* 22, no. 8 (1996): 959–977.

3. A. Manduca, P. J. Bayly, R. L. Ehman, et al., "MR Elastography: Principles, Guidelines, and Terminology," *Magnetic Resonance in Medicine* 85, no. 5 (2021): 2377–2390.

4. Y. Guo, S. Parthasarathy, P. Goyal, R. J. McCarthy, A. C. Larson, and F. H. Miller, "Magnetic Resonance Elastography and Acoustic Radiation Force Impulse for Staging Hepatic Fibrosis: A meta-Analysis," *Abdominal Imaging* 40, no. 4 (2015): 818–834.

5. P. Kennedy, M. Wagner, L. Castéra, et al., "Quantitative Elastography Methods in Liver Disease: Current Evidence and Future Directions," *Radiology* 286, no. 3 (2018): 738–763.

6. M. J. Korsmo, B. Ebrahimi, A. Eirin, et al., "Magnetic Resonance Elastography Noninvasively Detects in Vivo Renal Medullary Fibrosis

Secondary to Swine Renal Artery Stenosis," *Investigative Radiology* 48, no. 2 (2013): 61–68.

7. L. Warner, M. Yin, K. J. Glaser, et al., "Noninvasive in Vivo Assessment of Renal Tissue Elasticity During Graded Renal Ischemia Using MR Elastography," *Investigative Radiology* 46, no. 8 (2011): 509–514.

8. N. S. Shah, S. A. Kruse, D. J. Lager, et al., "Evaluation of Renal Parenchymal Disease in a Rat Model With Magnetic Resonance Elastography," *Magnetic Resonance in Medicine* 52, no. 1 (2004): 56–64.

9. O. Rouvière, R. Souchon, G. Pagnoux, and J.-M. Ménager, "MR Elastography of the Kidneys: Feasibility and Reproducibility in Young Healthy Adults," *Journal of Magnetic Resonance Imaging* 34, no. 4 (2011): 880–886.

10. G. Low, N. E. Owen, I. Joubert, et al., "Reliability of Magnetic Resonance Elastography Using Multislice two-Dimensional Spin-Echo Echo-Planar Imaging (SE-EPI) and Three-Dimensional Inversion Reconstruction for Assessing Renal Stiffness," *Journal of Magnetic Resonance Imaging* 42, no. 3 (2015): 844–850.

11. D. Gandhi, P. Kalra, B. Raterman, X. Mo, H. Dong, and A. Kolipaka, "Magnetic Resonance Elastography of Kidneys: SE-EPI MRE Reproducibility and Its Comparison to GRE MRE," *NMR in Biomedicine* 32, no. 11 (2019): e4141.

12. S. F. Bensamoun, L. Robert, G. E. Leclerc, L. Debernard, and F. Charleux, "Stiffness Imaging of the Kidney and Adjacent Abdominal Tissues Measured Simultaneously Using Magnetic Resonance Elastography," *Clinical Imaging* 35, no. 4 (2011): 284–287.

13. J. Chen, Z. Zhang, J. Liu, et al., "Multiparametric Magnetic Resonance Imaging of the Kidneys: Effects of Regional, Side, and Hydration Variations on Functional Quantifications," *Journal of Magnetic Resonance Imaging* 57, no. 5 (2023): 1576–1586.

14. S. R. Marticorena Garcia, M. Grossmann, S. T. Lang, et al., "Tomoelastography of the Native Kidney: Regional Variation and Physiological Effects on in Vivo Renal Stiffness," *Magnetic Resonance in Medicine* 79, no. 4 (2018): 2126–2134.

15. O. Rouvière, R. Souchon, G. Pagnoux, and J.-M. Ménager, "Magnetic Resonance Elastography of the Kidneys: Feasibility and Reproducibility in Young Healthy Adults," *Journal of Magnetic Resonance Imaging* 34, no. 4 (2011): 880–886.

16. M. Wagner, C. Besa, J. B. Ayache, et al., "MR Elastography of the Liver: Qualitative and Quantitative Comparison of Gradient Echo and Spin Echo Echoplanar Imaging Sequences," *Investigative Radiology* 51, no. 9 (2016): 575–581.

17. H. Knutsson, C.-F. Westin, and G. Granlund, "Local Multiscale Frequency and Bandwidth Estimation," Proceedings of the 1st International Conference on Image Processing, 1, (1994): 36–40.

18. H. Tzschätzsch, J. Guo, F. Dittmann, et al., "Tomoelastography by Multifrequency Wave Number Recovery From Time-Harmonic Propagating Shear Waves," *Medical Image Analysis* 30 (2016): 1–10.

19. K.-J. Streitberger, M. Reiss-Zimmermann, F. B. Freimann, et al., "High-Resolution Mechanical Imaging of Glioblastoma by Multifrequency Magnetic Resonance Elastography," *PLoS ONE* 9, no. 10 (2014): e110588.

20. D. Prezzi, R. Neji, C. Kelly-Morland, et al., "Characterization of Small Renal Tumors With Magnetic Resonance Elastography: A Feasibility Study," *Investigative Radiology* 53, no. 6 (2018): 344–351.

21. R. S. Brown, M. R. M. Sun, I. E. Stillman, T. L. Russell, S. E. Rosas, and J. L. Wei, "The Utility of Magnetic Resonance Imaging for Noninvasive Evaluation of Diabetic Nephropathy," *Nephrology, Dialysis, Transplantation* 35, no. 6 (2020): 970–978.

22. A. T. Güven, I. S. Idilman, C. Cebrayilov, et al., "Evaluation of Renal Fibrosis in Various Causes of Glomerulonephritis by MR Elastography: A Clinicopathologic Comparative Analysis," *Abdominal Radiology (NY)* 47, no. 1 (2022): 288–296.

23. J.-H. Han, J.-H. Ahn, and J.-S. Kim, "Magnetic Resonance Elastography for Evaluation of Renal Parenchyma in Chronic Kidney Disease: A Pilot Study," *Radiologia Medica* 125, no. 12 (2020): 1209–1215.

24. S. Aydin, S. Yildiz, I. Turkmen, et al., "Value of Shear Wave Elastography for Differentiating Benign and Malignant Renal Lesions," *Medical Ultrasonography* 1, no. 1 (2018): 21–26.

25. B. Chauveau, P. Merville, B. Soulabaille, et al., "Magnetic Resonance Elastography as Surrogate Marker of Interstitial Fibrosis in Kidney Transplantation: A Prospective Study," *Kidney360* 3, no. 11 (2022): 1924–1933.

26. J.-L. Gennisson, T. Deffieux, M. Fink, and M. Tanter, "Ultrasound Elastography: Principles and Techniques," *Diagnostic and Interventional Imaging* 94, no. 5 (2013): 487–495.

27. C. Nioche, F. Orlhac, S. Boughdad, et al., "LIFEx: A Freeware for Radiomic Feature Calculation in Multimodality Imaging to Accelerate Advances in the Characterization of Tumor Heterogeneity," *Cancer Research* 78, no. 16 (2018): 4786–4789.

28. D. G. Altman and J. M. Bland, "Measurement in Medicine: The Analysis of Method Comparison Studies," *Journal of the Royal Statistical Society: Series D (The Statistician)* 32, no. 3 (1983): 307–317.

29. T. Meyer, S. R. Marticorena Garcia, H. Tzschätzsch, et al., "Comparison of Inversion Methods in MR Elastography: An Open-Access Pipeline for Processing Multifrequency Shear-Wave Data and Demonstration in a Phantom, Human Kidneys, and Brain," *Magnetic Resonance in Medicine* 88, no. 4 (2022): 1840–1850.

30. J. Mura, F. Schrank, and I. Sack, "An Analytical Solution to the Dispersion-By-Inversion Problem in Magnetic Resonance Elastography," *Magnetic Resonance in Medicine* 84, no. 1 (2020): 61–71.

31. H.-M. Zhang, D.-G. Wen, J. Chen, et al., "A Diagnostic Test of Three-Dimensional Magnetic Resonance Elastography Imaging for Preoperative Prediction of Microvascular Invasion in Patients With T1 Stage Clear Cell Renal Carcinoma," *Translational Andrology and Urology* 12, no. 3 (2023): 466–476.

32. D. Le Bihan, S. Ichikawa, and U. Motosugi, "Diffusion and Intravoxel Incoherent Motion MR Imaging-Based Virtual Elastography: A Hypothesis-Generating Study in the Liver," *Radiology* 285, no. 2 (2017): 609–619.

33. S. Afat, J. Herrmann, H. Almansour, et al., "Acquisition Time Reduction of Diffusion-Weighted Liver Imaging Using Deep Learning Image Reconstruction," *Diagnostic and Interventional Imaging* 104, no. 4 (2023): 178–184.

34. M. C. Murphy, A. Manduca, J. D. Trzasko, K. J. Glaser, J. Huston, III, and R. L. Ehman, "Artificial Neural Networks for Stiffness Estimation in Magnetic Resonance Elastography," *Magnetic Resonance in Medicine* 80, no. 1 (2018): 351–360.

35. S. Ma, R. Wang, S. Qiu, et al., "MR Elastography With Optimization-Based Phase Unwrapping and Traveling Wave Expansion-Based Neural Network (TWENN)," *IEEE Transactions on Medical Imaging* 42, no. 9 (2023): 2631–2642.

36. M. McGarry, E. Van Houten, D. Sowinski, et al., "Mapping Heterogenous Anisotropic Tissue Mechanical Properties With Transverse Isotropic Nonlinear Inversion MR Elastography," *Medical Image Analysis* 78 (2022): 102432.